

General Strategy for Integrated SnO_2 /Metal Oxides as Biactive Lithium-Ion Battery Anodes with Ultralong Cycling Life

Jing Bai,^{†,‡} Baojuan Xi,^{*,‡} Zhenyu Feng,[‡] Junhao Zhang,[§] Jinkui Feng,^{||,ID} and Shenglin Xiong,^{*,‡,ID}

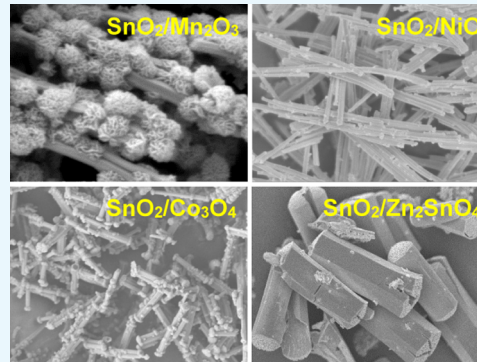
[†]State Key Laboratory of Crystal Materials and [‡]Key Laboratory for Colloid and Interface, Ministry of Education, & School of Chemistry and Chemical Engineering, Shandong University, Jinan, Shandong 250100, P. R. China

[§]School of Environmental and Chemical Engineering, Jiangsu University of Science and Technology, Zhenjiang, Jiangsu 212003, P. R. China

^{||}Key Laboratory for Liquid–Solid Structural Evolution & Processing of Materials (Ministry of Education), School of Materials Science and Engineering, Shandong University, Jinan, Shandong 250061, P. R. China

Supporting Information

ABSTRACT: Integration of bicomponents into a greater object or assemblage is a new avenue to acquire multifunctionality for metal oxide-based anodes for lithium-ion batteries (LIBs). Herein, we report a versatile means by which precursors serve as self-sacrificing templates to form architectures of SnO_2 phase and other metal oxides. The vital challenge is the determination of appropriate synthetic system that can benefit the formation of respective precursors in a structure or single-source precursors of tin and other metal species. In the current work, by the aids of synergy action between L-proline and ethylene glycol (EG), precursors containing two metal ions are generally fabricated. Adequate flexibility of the present method has been achieved for $\text{SnO}_2/\text{M}_x\text{O}_y$ hierarchical hybrids, including Mn_2O_3 , Co_3O_4 , NiO , and Zn_2SnO_4 , by calcination of their corresponding SnMn , SnCo , SnNi , and SnZn precursors, respectively. When evaluated as anode materials for LIBs, the obtained $\text{SnO}_2/\text{M}_2\text{O}_3$ homogeneous hybrids, as expected, show higher specific capacity and ultralong cycling stability, gaining a reversible specific capacity of $610.3 \text{ mA h g}^{-1}$ after 600 cycles with only decay of 0.29 mA h g^{-1} per cycle at 1 A g^{-1} and 487 mA h g^{-1} after 1001 cycles at a high current density of 2 A g^{-1} .



INTRODUCTION

As one of the excellent energy storage carriers, lithium-ion batteries (LIBs) have drawn extensive attention in the past decades because of the broad range of applications in mobile electric devices, hybrid electric vehicles, and smart grids.^{1–6} To fulfill the higher requirements of these applications, further improvements in terms of specific capacity and cycling life should be initiated. Because of their intrinsic limitations in performance, bulk electrode materials fail to completely meet the ever-growing demands. It has been widely demonstrated that nanosized anode/cathode materials enable better rate capability and capacity via reducing diffusion distances of lithium ions and augmenting the contact area between the electrolyte and the electrode. In addition, the commercial graphite anode exhibits a low theoretical capacity (372 mA h g^{-1}),^{7,8} which cannot keep pace with the increasing need for energy density of those apparatus with LIB as a power source. In response, metal oxides with higher theoretical capacity (e.g., SnO_2 ,^{9,10} Co_3O_4 ,¹¹ MnO_2 ,^{12–14} Fe_2O_3 ,¹⁵ and ZnCo_2O_4 ¹⁶) have been emerging as attractive anode candidates for LIBs. However, they usually show poor cycling stability and rate capability resulting from low conductivity and remarkable volume change during the charge/discharge process.^{9–19} To solve the above issues, it is a useful strategy to assemble two

kinds of metal oxides with nanosize into hierarchical composites.^{20–22}

Recently, such bicomponent hybrids featured with the complex heterostructure have been developed and designed to serve as active materials for LIBs, verifying that these hybrid anodes are furnished with better lithium storage property (higher specific capacity, better cycling stability, etc.) than any corresponding counterparts.^{20–22} From the viewpoint of structural modeling, one representative pattern is that two components heterogeneously dispersed in the structure and can be clearly differentiated due to their definite boundary between each other, such as $\text{ZnO}@\alpha\text{-Co(OH)}_2$ core–shell structures featured by ZnO spheres as core and $\alpha\text{-Co(OH)}_2$ nanosheets as shell²³ and $\alpha\text{-Fe}_2\text{O}_3/\text{SnO}_2$ heterostructures^{24,25} consisting of SnO_2 nanowire stem with sixfold $\alpha\text{-Fe}_2\text{O}_3$ nanorod branches and SnO_2 nanosheet base growing with branched Fe_2O_3 nanorods. Two steps are versatility applied to sequentially generate the two components or precursors into such hybrid architectures with one material as matrix for the growth of another. Another appealing motif is the homogeneous

Received: August 7, 2017

Accepted: September 22, 2017

Published: October 5, 2017



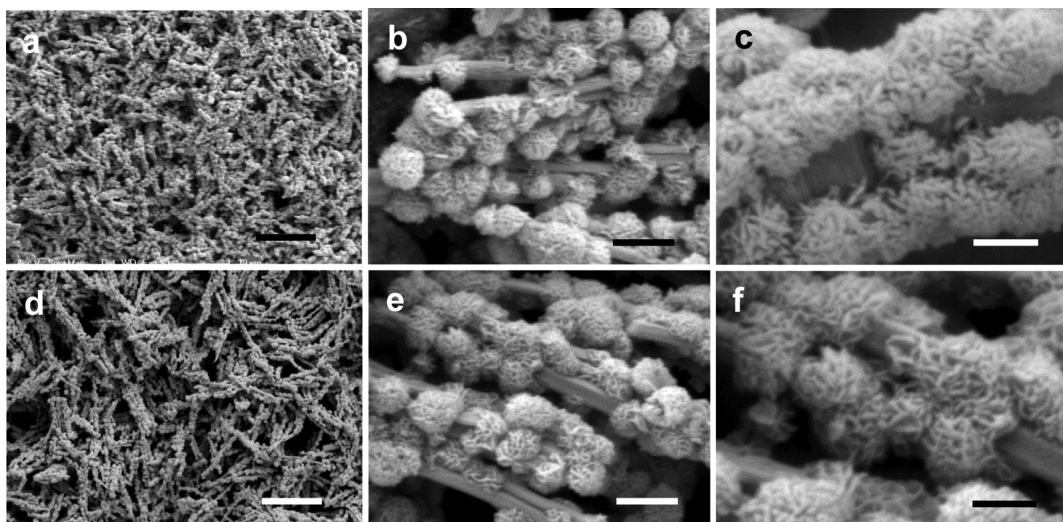


Figure 1. FESEM images at different resolutions of the SnMn precursor (a–c) and $\text{SnO}_2/\text{Mn}_2\text{O}_3$ HHs (d,e). Scale bar: (a) 10 μm , (b) 1 μm , (c) 500 nm, (d) 10 μm , (e) 1 μm , and (f) 500 nm.

dispersion of components in the entire heterostructure.^{26–28} The Yuan group reported the $\text{ZnO}/\text{ZnFe}_2\text{O}_4$ submicrocubes constructed with well-dispersed subunits of two oxides by calcination of Prussian blue analogue of $\text{Zn}_3[\text{Fe}(\text{CN})_6]_2$ cubes, demonstrating better electrochemical Li storage performance.²⁶ CoO/ CoFe_2O_4 nanocomposites had been derived from CoFe-layered double hydroxides, exhibiting a tunable lithium storage property by changing the ratio of the component metal oxides.²⁷ In the connection, one of the challenging issues is to obtain single-resource precursors involving two active metals. Despite great efforts, the effective and general synthesis was largely prohibited by the difficulty of epitaxial growth of the second kind of materials or the limited range of such single sources of bimetal precursors as Prussian blue. Moreover, the aforementioned composites cannot tolerate long cycling at higher current density, probably pertaining to the lack of proper conjoint components. Therefore, efficient coupling of bimetals in a versatile synthetic system should be initiated immediately targeted at high-performance anode materials for LIBs.

Motivated by the advantages of bioxide composites, the general one-pot synthesis of such hybrids was realized in our work by picking a suitable couple of solvent and ligand. This was the first time to enable the architectures of nanosized SnO_2 phase and other oxides including Mn_2O_3 , Co_3O_4 , NiO , and Zn_2SnO_4 . By rationally picking up the powerful linker and solvent to conjugate tin and other metal species, hierarchical structures composed of single- or double-source precursors were obtained depending on the intrinsic property of metal ions, which played the key role in the synthesis of bioxide composites. Particularly, $\text{SnO}_2/\text{Mn}_2\text{O}_3$ hierachial hybrids (HHs) consisted of nanosheet networks attached to the nanorod stem. When $\text{SnO}_2/\text{Mn}_2\text{O}_3$ HHs worked as the anode materials for LIBs, a reversible capacity of 487 mA h g^{-1} was maintained even after a long 1000 cycles at a high current density of 2 A g^{-1} , which was much better than $\text{SnO}_2/\text{Mn}_2\text{O}_3$ submicrorods and pristine Mn_2O_3 . The origin of performance elevation could be attributed to the synergistic effect of nanohybrid, structural interface, and void among the nanosheets. This strategy displays adequate versatility for architectures of advanced oxide-based hybrid anodes for LIBs and supercapacitors.

RESULTS AND DISCUSSION

The overall morphology and structure are investigated by the field emission scanning electron microscopy (FESEM) technique. Figure 1a demonstrates a high yield of the SnMn precursor. To be more detailed (Figure 1b,c), some assemblages bind to the submicrorod stem similar to agaric growing on trees. Thereinto, submicrorods are about 5–10 μm in length. Moreover, these assemblages are assembled with interconnected nanosheets, leaving significant voids. According to the thermogravimetric analysis (TGA) result (Figure S1 in the Supporting Information), the precursor was annealed above 500 °C to transform completely into $\text{SnO}_2/\text{Mn}_2\text{O}_3$ HHs. As shown in Figure 1d–f, the morphology and structure of $\text{SnO}_2/\text{Mn}_2\text{O}_3$ HHs inherited well from the paternal template.

The transmission electron microscopy (TEM) technique was applied to visualize the detailed structure information. In Figure 2a,b, for SnMn precursor, it is clearly exhibited that the thin nanosheets constitute flowerlike clusters which are grown on the submicrorod stem. The TEM images of $\text{SnO}_2/\text{Mn}_2\text{O}_3$ HHs are displayed in Figure 2c,d, demonstrating the structural feature inherent from their precursors. The high-resolution TEM (HRTEM) image of Figure 2e is used to detect the crystalline nature of $\text{SnO}_2/\text{Mn}_2\text{O}_3$ HHs. Furthermore, the faster Fourier transformation electron diffraction (FFT-ED) pattern was recorded from the square area of Figure 2e, exhibiting the well-defined diffraction spots. After calculation and analysis, the sets of diffractions are indexed to be (020) and (211) of cubic Mn_2O_3 with lattice spacings of 0.47 and 0.39 nm, respectively. Another HRTEM image in Figure 2f was also recorded from $\text{SnO}_2/\text{Mn}_2\text{O}_3$ HHs. The FFT-ED pattern from the marked square can be indexed to be two sets of diffraction spots, one of which is corresponding to cubic Mn_2O_3 labeled by a parallelogram and another spot marked by a circle is calculated to be related with the (101) plane of tetragonal SnO_2 . At the same time, the elemental configuration is sharply visualized by a scanning transmission electron microscopy (STEM) instrument, where the mapping images in Figure 2g describe the distribution of Mn and Sn mainly focusing on assemblages and submicrorod stems, respectively. The phase of the annealed sample was confirmed by the X-ray diffraction (XRD) pattern in Figure 3a. They can be well-indexed to be

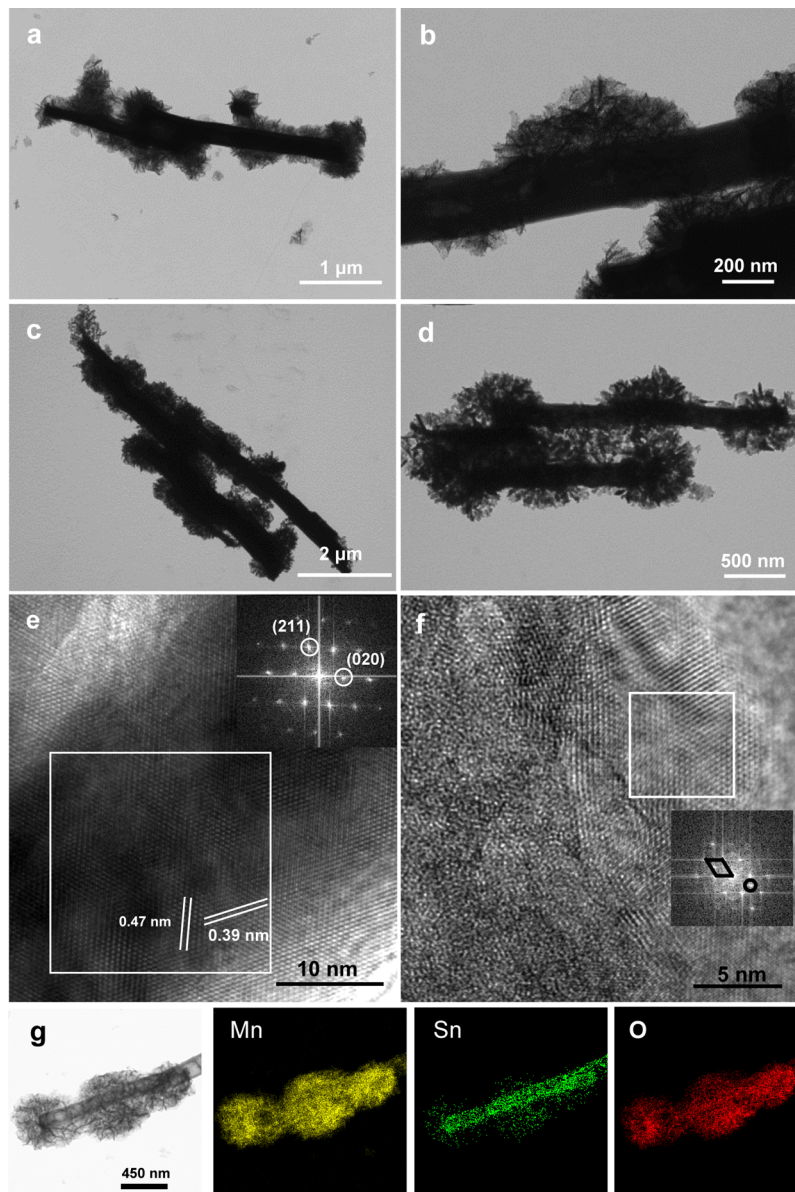


Figure 2. TEM images of (a,b) SnMn precursor and (c,d) $\text{SnO}_2/\text{Mn}_2\text{O}_3$ HHs; (e,f) HRTEM images from $\text{SnO}_2/\text{Mn}_2\text{O}_3$ HHs and (g) corresponding elemental mapping images of Mn, Sn, and O for one single $\text{SnO}_2/\text{Mn}_2\text{O}_3$ HH.

tetragonal SnO_2 (JCPDS no. 41-1445) and cubic Mn_2O_3 (JCPDS no. 41-1442) marked in the pattern. There is no peak for impurity, indicating the high purity of the product.

To verify the multifunctionality of the synthetic system in the present method in regard of incorporating two metal species into the precursors, we used $\text{Co}(\text{CH}_3\text{COO})_2 \cdot 4\text{H}_2\text{O}$, $\text{Ni}(\text{CH}_3\text{COO})_2 \cdot 4\text{H}_2\text{O}$, and $\text{Zn}(\text{CH}_3\text{COO})_2 \cdot 2\text{H}_2\text{O}$ to substitute the previous $\text{Mn}(\text{CH}_3\text{COO})_2 \cdot 4\text{H}_2\text{O}$ for study and successfully fabricated their corresponding precursors which were nominated as SnCo, SnNi, and SnZn precursors, respectively. As shown in Figure S2, these precursors were profiled by similar XRD patterns with well-defined peaks, demonstrating good crystallinity. After calcination at 500 or 600 °C, various $\text{SnO}_2/\text{oxides}$ HHs were harvested, which were analyzed via the XRD technique in Figure 3. Specifically, the XRD pattern in Figure 3b of $\text{SnO}_2/\text{Co}_3\text{O}_4$ HHs can be indexed to tetragonal SnO_2 (JCPDS 41-1445) and cubic Co_3O_4 (JCPDS 42-1467). Simultaneously, other hierarchical hybrids (HHs) of $\text{SnO}_2/$

NiO and $\text{SnO}_2/\text{Zn}_2\text{SnO}_4$ can effectively be identified by XRD patterns in Figure 3c,d, namely, tetragonal SnO_2 (JCPDS 41-1445), cubic NiO ($Fm\bar{3}m$, JCPDS 47-1049), and cubic Zn_2SnO_4 (JCPDS 24-1470). These XRD results confirmed the formation of various $\text{SnO}_2/\text{oxide}$ hybrids, implying the versatility of the present method.

The FESEM image in Figure 4a captures a panoramic sight of $\text{SnO}_2/\text{Co}_3\text{O}_4$ HHs, which displays the screw-nut-like structures that are clearly observed from Figure 4b. It is clear that the caps are attached at both ends, and some discrete nanoparticles bind on the rodlike stem. Furthermore, the microstructure details of SnO_2/NiO HHs were also inspected. Figure 4c remarkably describes the typical one-dimensional structures. On the basis of the observation from the higher-magnification FESEM image in Figure 4d, several nanorods are preferentially stacked into bundles with a few nanoparticles scattered onto the nanorod surface. When $\text{Zn}(\text{CH}_3\text{COO})_2 \cdot 2\text{H}_2\text{O}$ replaced $\text{Mn}(\text{CH}_3\text{COO})_2 \cdot 4\text{H}_2\text{O}$ in our synthesis, final

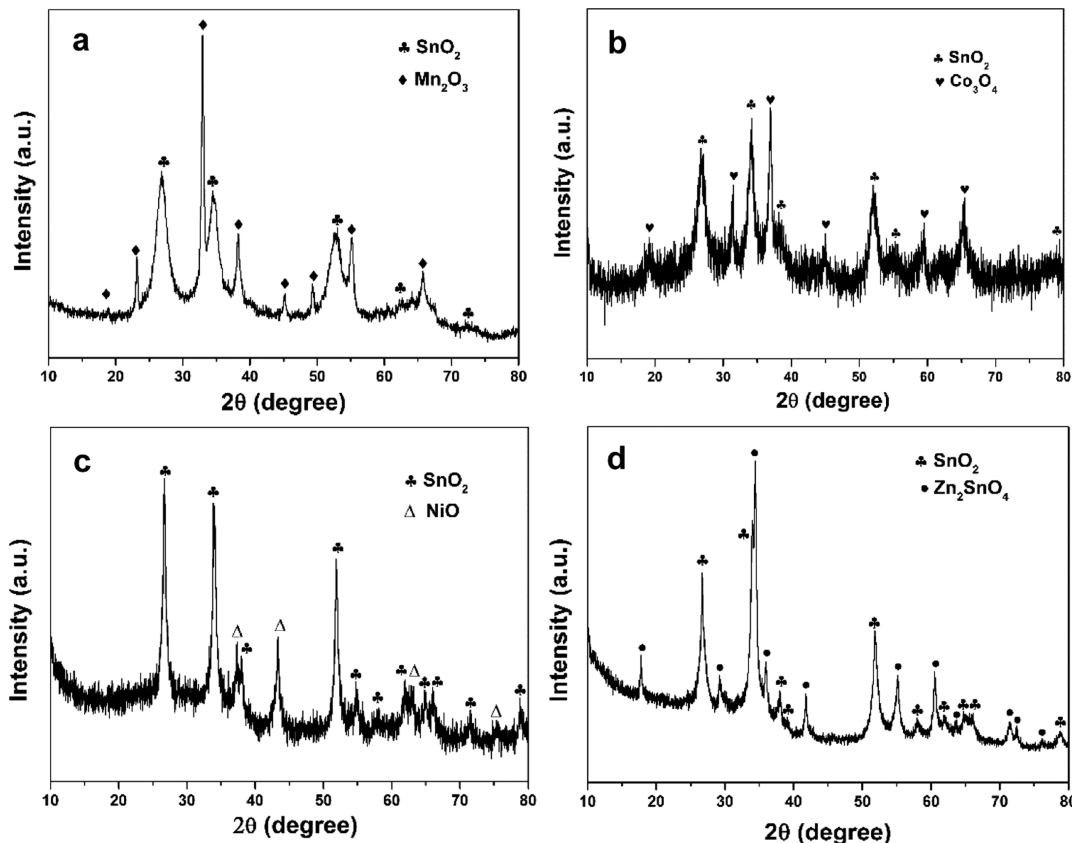


Figure 3. XRD patterns of (a) SnO₂/Mn₂O₃ HHs, (b) SnO₂/Co₃O₄ HHs, (c) SnO₂/NiO HHs, and (d) SnO₂/Zn₂SnO₄ HHs.

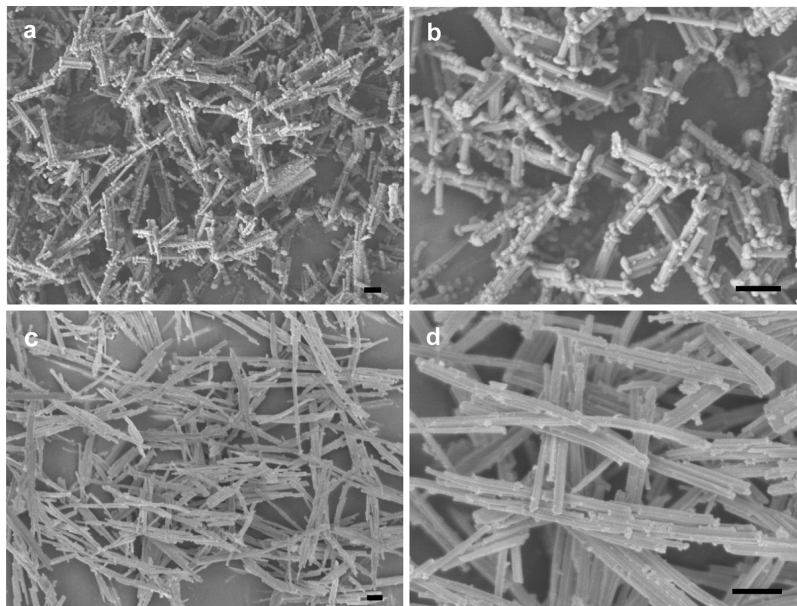


Figure 4. FESEM images of SnO₂/Co₃O₄ HHs (a,b) and SnO₂/NiO HHs (c,d). Scale bar: 1 μ m for all panels.

SnO₂/Zn₂SnO₄ HHs were transformed from the precursor. It is interesting to note that SnO₂/Zn₂SnO₄ HHs still maintain one-dimensional structures but hexagonal prisms, as indicated in Figure 5a,b. Because of sintering at high temperature, some prisms suffer from cracking pointed by arrows. The mapping description in Figure 5c gives the elemental distribution of Zn and Sn, implying the uniform dispersion of SnO₂ and Zn₂SnO₄ domains over the whole hexagonal prism.

To shed light on the formation mechanism of precursors, some tests and related analyses were done. In the XRD pattern of the SnMn precursor in Figure S2, the appearance of the peak at about 10.8° demonstrates the formation of a glycolate precursor.²⁹ A control experiment was carried out where K₂SnO₃·3H₂O was not applied with other conditions being kept constant, and finally, flowerlike Mn-glycolate was obtained, as shown in Figure S3. After heat treatment, pristine

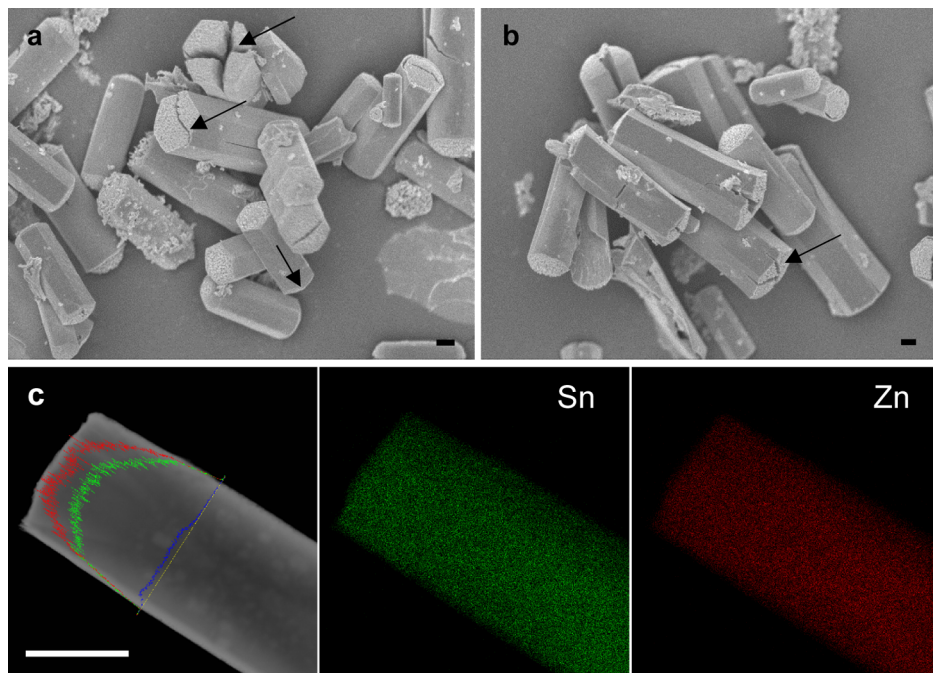


Figure 5. (a,b) FESEM images of $\text{SnO}_2/\text{Zn}_2\text{SnO}_4$ HHs and (c) TEM image recorded from a typical single $\text{SnO}_2/\text{Zn}_2\text{SnO}_4$ hexagonal prism and the corresponding elemental mapping images (c) of Sn and Zn. Scale bars: (a,b) 1 μm and (c) 2 μm .

Mn_2O_3 was attained and indexed by the XRD pattern in Figure S4. Similarly, if $\text{Mn}(\text{CH}_3\text{COO})_2 \cdot 4\text{H}_2\text{O}$ was not added, no product was harvested. The comparative results implied that Mn was inclined to bond with EG but not with L-proline and had higher coordination ability to bond with EG than Sn. Hence, it is reasonable to speculate that the SnMn precursor was composed of Mn-glycolate and Sn-proline. To obtain more information about the precursor, Fourier transform infrared (FTIR) spectra of L-proline and SnMn precursor were recorded in Figure S5. A remarkable band at 3433 cm^{-1} in both spectra implies the occurrence of hydroxyl vibration. In the spectrum of the SnMn precursor, the bands at 2934 , 2895 , and 2837 cm^{-1} are related to the asymmetric stretching vibration of N-H and C-H groups.³⁰ It should be noted that the C=O stretch band for the carboxyl group of L-proline appeared at 1623 cm^{-1} and disappeared in the spectrum of the precursor.^{31,32} There are two new bands at 1633 and 1462 cm^{-1} ascribed to the asymmetric $\nu_{\text{as}}(\text{COO}^-)$ and symmetric $\nu_s(\text{COO}^-)$ stretching of carboxyl groups, respectively. According to the wavenumber separation value (D) between the $\nu_{\text{as}}(\text{COO}^-)$ and $\nu_s(\text{COO}^-)$ bands, the type of interaction between the carboxylate head and metal ions can be distinguished as monodentate, bidentate bridging, bidentate chelating, or ionic interaction.^{32–34} Here, the D value is 171 cm^{-1} , suggesting that the carboxyl groups play a role in bidentate bridging.^{32–34} Thereafter, the Sn-proline complex is described as $\text{Sn}-\text{O}-\text{C}(\text{R})-\text{O}-\text{Sn}$ in which L-proline bridges two Sn atoms at each end. Some unsaturated Mn atoms in Mn-glycolate and Sn atoms in Sn-proline would bond with the carboxyl of Sn-proline and hydroxyl of Mn-glycolate, which rendered the hybridization of SnMn precursor HHs. When $\text{Zn}(\text{CH}_3\text{COO})_2 \cdot 2\text{H}_2\text{O}$ was used in the synthetic system, the as-attained SnZn precursor exhibited well-shaped hexagonal prisms. Moreover, the characteristic XRD peak corresponding to the metal glycolate disappears. Correspondingly, the SnZn precursor is inferred to be a single-source analogue of the

SnZn-proline complex. After calcination at high temperature, it completely transformed into SnO_2 and ZnSn_2O_4 , similar to the reported Prussian blue-structured $\text{Zn}_3[\text{Fe}(\text{CN})_6]_2$ as a template to fabricate ZnO and ZnFe_2O_4 components.²⁶ These precursors, including SnMn, SnCo, SnNi, and SnZn precursors, showed prominently different coordination properties and crystallization behaviors to get different structure bimetal oxides, which mainly originated from the different intrinsic properties of cations, that is, Mn^{2+} , Co^{2+} , Ni^{2+} , and Zn^{2+} . A more comprehensive and extensive investigation into the underlying fundamentals for such distinctions with changing metal cations is undergoing. From the above discussion, the significance of synthetic system was highlighted. The option of appropriate system can moderate the hybridization fashion and determine the realization of final hybridization.

To prove the superiority of such hierarchical structures as the anode materials, another control sample of $\text{SnO}_2/\text{Mn}_2\text{O}_3$ submicrorods was attained from its precursor via calcination. As can be seen in Figure S6a, the FESEM image of the precursor of $\text{SnO}_2/\text{Mn}_2\text{O}_3$ submicrorods describes a rodlike structure with a length of $2\text{--}8\text{ }\mu\text{m}$ and a diameter of hundred nanometers to several micrometers. Moreover, this morphology was maintained after annealing, as demonstrated in Figure S6b. The XRD pattern of $\text{SnO}_2/\text{Mn}_2\text{O}_3$ submicrorods in Figure S7 offers a similar profile, which is determined to be tetragonal SnO_2 (JCPDS no. 41-1445) and cubic Mn_2O_3 (JCPDS no. 41-1442). Further confirmation of chemical composition was given by the STEM mapping results (Figure S6c), evidently demonstrating the homogeneous distribution of Sn, Mn, and O throughout the rodlike structure.

When tested as an anode material for LIBs, the electrochemical behaviors of several samples were characterized. As shown in Figure 6a, both $\text{SnO}_2/\text{Mn}_2\text{O}_3$ HHs and submicrorods exhibit good rate capability. At the low current densities of 0.2 , 0.5 , and 1 A g^{-1} , the capacity of $\text{SnO}_2/\text{Mn}_2\text{O}_3$ HHs is a little higher than that of the submicrorods. However, when the

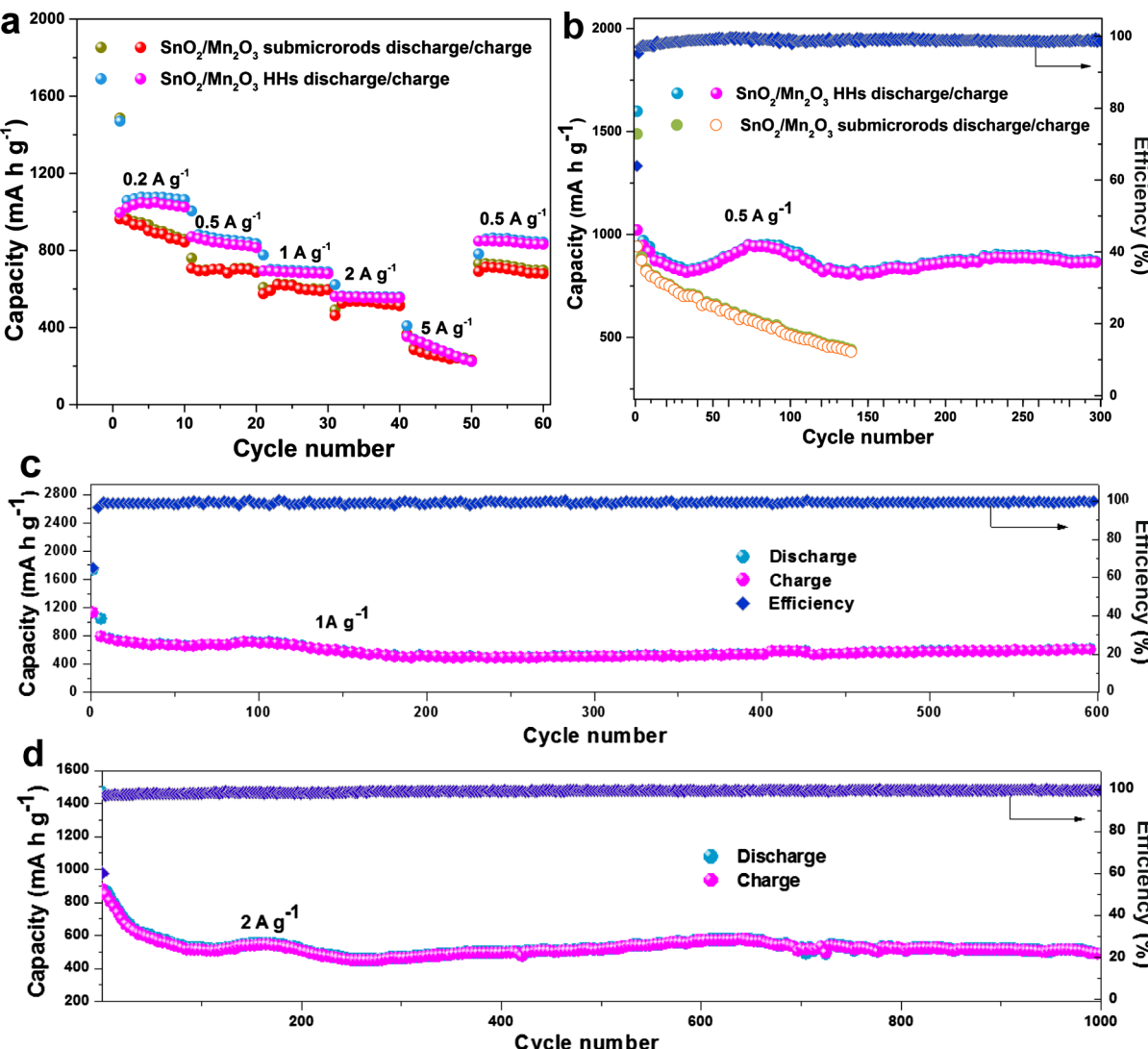


Figure 6. (a) Rate capability and (b) cycling performance of $\text{SnO}_2/\text{Mn}_2\text{O}_3$ HHs and submicrorods at a current density of 0.5 A g^{-1} and (c,d) cycling performance of $\text{SnO}_2/\text{Mn}_2\text{O}_3$ HHs at current densities of 1 and 2 A g^{-1} , respectively.

current density increases to 2 and 5 A g^{-1} , both samples offer a similar reversible capacity. As the rate is back to 0.5 A g^{-1} in Figure S8, the specific capacity of $\text{SnO}_2/\text{Mn}_2\text{O}_3$ HHs is $859.2 \text{ mA h g}^{-1}$ and is comparable with that of 814 mA h g^{-1} at the initial current density of 0.5 A g^{-1} , indicating a good rate capacity of the active material. The reversible capacity can be still maintained as high as $839.9 \text{ mA h g}^{-1}$ after 260 cycles. However, $\text{SnO}_2/\text{Mn}_2\text{O}_3$ submicrorods rapidly degrade to about 400 mA h g^{-1} just at 140th cycle.

Figure S9 shows the cyclic voltammetry (CV) curves of $\text{SnO}_2/\text{Mn}_2\text{O}_3$ HHs at a scan rate of 0.1 mV s^{-1} in the potential range of 0.01 – 3.0 V . In the first cathodic process, a weak and broad cathodic peak was located at around 1.26 V but disappeared in the successive cycles, which can be attributed to the reduction of Mn^{3+} to Mn^{2+} .^{35,36} The main cathodic peak at around 0.96 V is ascribed to the reduction of SnO_2 to Sn and Li_2O .³⁷ The last main peak located at 0.24 V is associated with the reduction of Mn^{2+} to Mn^0 and the alloying reaction of Sn and Li^+ (Li_xSn).^{35,36,38,39} In the anodic process, the anodic peak at 0.56 V is for the oxidation of Li_xSn alloy to Sn .³⁸ The anodic peak at 1.27 V is ascribed to the oxidation of Mn^0 to Mn^{2+} and Sn^0 partially back to SnO_2 .^{40,41} In the second scan, the cathodic

peak at 0.96 V weakens and then vanishes subsequently, suggesting an irreversible transition of SnO_2 to Sn .^{37,41} Other two peaks at ~ 0.44 and 0.06 V are attributed to the reduction of Mn^{2+} to Mn^0 and the formation of an Li_xSn alloy, respectively.^{35,36,39}

Here, the cycling performance of the as-prepared samples at different current densities was also studied. First, at the current density of 0.5 A g^{-1} in Figure 6b, the initial discharge capacity and charge capacity of $\text{SnO}_2/\text{Mn}_2\text{O}_3$ HHs are 1598.7 and $1021.4 \text{ mA h g}^{-1}$, respectively. The significant capacity loss of $577.3 \text{ mA h g}^{-1}$ is generally considered to be caused by the formation of a solid electrolyte interphase (SEI) layer on the surface of anode materials in the first discharge process.^{42–47} Subsequently, the capacity profile undergoes declination followed by inclination, which is familiarly observed for transition metal oxides. This phenomenon generally results from the reversible formation of the gel-like polymeric layer.^{48–53} This process was recognized as the activation stage. Even after 300 cycles, $\text{SnO}_2/\text{Mn}_2\text{O}_3$ HHs could maintain stable capacity, delivering $867.8 \text{ mA h g}^{-1}$, whereas $\text{SnO}_2/\text{Mn}_2\text{O}_3$ submicrorods show a trend of capacity down all the way and just recover 428 mA h g^{-1} at the 140th cycle. When the

cycling performance of $\text{SnO}_2/\text{Mn}_2\text{O}_3$ HHs is tested at the current density of 1 A g^{-1} (Figure 6c), the first discharge and charge capacities are 1734.9 and 1126 mA h g^{-1} , respectively, with a high initial coulombic efficiency of 65%. The irreversible capacity can be attributed to the decomposition of the electrolyte to form a SEI layer on the surface of the electrode.^{42–47} From the sixth cycle onward, the electrode shows an excellent stable capacity, and the reversible capacity of $\text{SnO}_2/\text{Mn}_2\text{O}_3$ HHs is $610.3 \text{ mA h g}^{-1}$ after 600 cycles with only a slight decay of 0.29 mA h g^{-1} per cycle. By comparison, as displayed in Figure S10a, the first discharge and charge capacities of $\text{SnO}_2/\text{Mn}_2\text{O}_3$ submicrorods and pristine Mn_2O_3 are 1519.5 and 1028.5 as well as 933.7 and $526.1 \text{ mA h g}^{-1}$ at a current density of 1 A g^{-1} . After lithium storage cycling, the reversible capacity of both samples degrades to 192.6 at 250th cycle and $290.4 \text{ mA h g}^{-1}$ at 100th cycle. When the current density increases to 2 A g^{-1} (Figure 6d), $\text{SnO}_2/\text{Mn}_2\text{O}_3$ HHs can still maintain a good cycling performance, which additionally suggests a remarkable rapid charging ability. It delivers a reversible capacity as high as 487 mA h g^{-1} after 1001 cycles. The other two electrodes made of $\text{SnO}_2/\text{Mn}_2\text{O}_3$ submicrorods and pristine Mn_2O_3 cannot endure long cycling at such a high current density. From Figure S10, the reversible capacities of the former electrode are only 192.6 and 115 mA h g^{-1} after 250 cycles at the current densities of 1 and 2 A g^{-1} , respectively, recovering about 12.7 and 7.6% from the first discharge capacity. In addition, the latter one experiences 100 lithiation/delithiation cycles, and the charge capacities reduce to 290.4 and $202.7 \text{ mA h g}^{-1}$ at the current densities of 1 and 2 A g^{-1} , respectively.

On the basis of the above data and analyses, it was well-concluded that $\text{SnO}_2/\text{Mn}_2\text{O}_3$ HHs exhibited a superior rate capability and cycling life to $\text{SnO}_2/\text{Mn}_2\text{O}_3$ submicrorods and pristine Mn_2O_3 . Through the structural and compositional comparison among them, the superiority of $\text{SnO}_2/\text{Mn}_2\text{O}_3$ HHs can be analyzed as follows. The nanosheet-interconnecting network could raise the surface area of the electrode materials, favorably increasing the contact area between the electrode and the electrolyte and allowing the full occurrence of electrochemical reactions, demonstrated a better performance of $\text{SnO}_2/\text{Mn}_2\text{O}_3$ HHs than the submicrorods. What is more, the structural voids benefited buffering the volumetric variation of the active materials during the repeated discharge/charge process. Last, the synergistic effect of SnO_2 and Mn_2O_3 was another dominating reason to enhance the electrochemical performance of the composite,⁵⁴ which was verified by the worse lithium storage property of the single-phase Mn_2O_3 .

CONCLUSIONS

In summary, the general fabrication of integrated $\text{SnO}_2/\text{metal oxide}$ HHs has been devised based on the template-directing route, including Mn_2O_3 , Co_3O_4 , NiO , and Zn_2SnO_4 as the oxide phase. Their corresponding precursors containing tin and another metal were successfully designed by taking advantage of the synergistic role of L-proline and EG. By analyzing the phase and bond information via XRD and FTIR, single- or double-source precursors could be engineered depending on the coordination and/or intrinsic property of different metal species. In principle, the synthetic strategy is applicable to the integration of other metal oxides. Thereinto, $\text{SnO}_2/\text{Mn}_2\text{O}_3$ HHs were featured as architectural hybrids with flowerlike clusters anchoring on the rod stem. In accordance with our present work, $\text{SnO}_2/\text{Mn}_2\text{O}_3$ HHs as the anode material for

LIBs showed the enhanced storage capacity and cycling stability. The superior electrochemical performance of $\text{SnO}_2/\text{Mn}_2\text{O}_3$ HHs could be attributed to their special nanohybrid hierarchical architecture. It proved once more that the reasonable design of nanoarchitectures showed an encouraging avenue to improve the performance of anode materials for LIBs.

MATERIALS AND METHODS

Synthesis of $\text{SnO}_2/\text{Mn}_2\text{O}_3$ HHs. All chemical reagents were used as received without any further purification. The synthesis of the $\text{SnO}_2/\text{Mn}_2\text{O}_3$ hybrid precursor (SnMn precursor) was conducted by a simple refluxing method. In a typical synthesis, 1 mmol $\text{Mn}(\text{CH}_3\text{COO})_2 \cdot 4\text{H}_2\text{O}$, 0.5 mmol $\text{K}_2\text{SnO}_3 \cdot 3\text{H}_2\text{O}$, and 1 mmol L-proline were dispersed into 40 mL of EG and oil-bathed in a one-neck capped flask connected with a condenser at 170°C for 6 h under continuous stirring. After being cooled to room temperature naturally, the product was centrifuged, washed with ethanol several times, and then dried at 60°C overnight to obtain brown powder. Subsequently, the precursor was calcined at 500°C for 5 h in an air atmosphere with the heating rate of $2^\circ\text{C}/\text{min}$. Finally, the dark brown $\text{SnO}_2/\text{Mn}_2\text{O}_3$ HHs were obtained.

Synthesis of $\text{SnO}_2/\text{Co}_3\text{O}_4$ HHs. The synthetic procedures were similar to those of $\text{SnO}_2/\text{Mn}_2\text{O}_3$ HHs except that $\text{Mn}(\text{CH}_3\text{COO})_2 \cdot 4\text{H}_2\text{O}$ was replaced with 1 mmol $\text{Co}(\text{CH}_3\text{COO})_2 \cdot 4\text{H}_2\text{O}$ in the experiment.

Synthesis of SnO_2/NiO HHs. The synthetic procedures were similar to those of $\text{SnO}_2/\text{Mn}_2\text{O}_3$ HHs except that $\text{Mn}(\text{CH}_3\text{COO})_2 \cdot 4\text{H}_2\text{O}$ was replaced with 1 mmol $\text{Ni}(\text{CH}_3\text{COO})_2 \cdot 4\text{H}_2\text{O}$ in the experiment.

Synthesis of $\text{SnO}_2/\text{Zn}_2\text{SnO}_4$ HHs. The synthetic procedures were similar to those of $\text{SnO}_2/\text{Mn}_2\text{O}_3$ HHs except that $\text{Mn}(\text{CH}_3\text{COO})_2 \cdot 4\text{H}_2\text{O}$ was replaced with 0.5 mmol $\text{Zn}(\text{CH}_3\text{COO})_2 \cdot 2\text{H}_2\text{O}$ in the experiment, and the corresponding precursor was annealed at 600°C .

Synthesis of Mn_2O_3 Nanosheets. The synthetic procedures were similar to those of $\text{SnO}_2/\text{Mn}_2\text{O}_3$ HHs except that $\text{K}_2\text{SnO}_3 \cdot 3\text{H}_2\text{O}$ was not applied in the experiment.

Synthesis of $\text{SnO}_2/\text{Mn}_2\text{O}_3$ Submicrorods. The synthetic procedures were similar to those of $\text{SnO}_2/\text{Mn}_2\text{O}_3$ HHs except that the flask was opened and not connected with the condenser when oil-bathing the reagents.

Characterization of Materials. The phase detection of products was performed by powder XRD (Philips X'Pert Pro Super diffractometer, Cu K α radiation, $\lambda = 1.54178 \text{ \AA}$). TEM and FESEM images were recorded with a transmission electron microscope (JEOL, JEM-1011) and a field emission scanning electron microscope (JEOL, JSM-6700F), respectively. HRTEM images were recorded using an electron microscope (JEM-2100F, accelerating voltage: 200 kV) coupled with an X-ray energy-dispersive spectroscopy (EDX) instrument. TGA (PerkinElmer Diamond TG/DTA apparatus) was conducted at a heating rate of $10^\circ\text{C}/\text{min}$ in flowing air. FTIR spectra were recorded on a Bruker EQUINOX55 spectrometer with a potassium bromide pellet as a control.

Electrochemical Characterization. The working electrode was made of 70 wt % active material, 20 wt % conductive material (acetylene black), and 10 wt % binder (carboxymethylcellulose sodium). The above materials were mixed with water by grinding to form a slurry, which was then pasted on the pure copper foil and dried at 80°C in vacuum. The obtained foil was cut into a disk with a diameter of 12 mm, and

the mass density of the active material was about 1 mg cm⁻². The electrochemical measurements were performed using CR2032 coin cells in the voltage range of 3.0–0.01 V. The cells were assembled in an argon-filled glovebox with the lithium foil as the counter electrode and the Celgard 2400 membrane as the separator. The electrolyte was a mixture of 1 M LiPF₆ in ethylene carbonate, dimethyl carbonate, and diethyl carbonate in a volume ratio of 1:1:1 purchased from Samsung Chemical Corporation.

■ ASSOCIATED CONTENT

Supporting Information

The Supporting Information is available free of charge on the ACS Publications website at DOI: [10.1021/acsomega.7b01146](https://doi.org/10.1021/acsomega.7b01146).

TGA, XRD, FESEM, FTIR, and TEM images of the corresponding precursors and the final products and electrochemical performance of SnO₂/Mn₂O₃ HHs and submicrorods ([PDF](#))

■ AUTHOR INFORMATION

Corresponding Authors

*E-mail: baojuanxi@sdu.edu.cn (B.X.).

*E-mail: chexsl@sdu.edu.cn (S.X.).

ORCID

Jinkui Feng: [0000-0002-5683-849X](https://orcid.org/0000-0002-5683-849X)

Shenglin Xiong: [0000-0002-8324-4160](https://orcid.org/0000-0002-8324-4160)

Notes

The authors declare no competing financial interest.

■ ACKNOWLEDGMENTS

The authors gratefully acknowledge the financial support provided by the National Natural Science Fund of China (nos. 21601108 and 21371108), the Fundamental Research Funds of Shandong University (no. 2016JC033 and 2016GN010), Young Scholars Program of Shandong University (no. 2017WLJH15), and the Taishan Scholar Project of Shandong Province (no. ts201511004).

■ REFERENCES

- (1) Yu, Y.; Chen, C.-H.; Shui, J.-L.; Xie, S. Nickel-Foam-Supported Reticular CoO-Li₂O Composite Anode Materials for Lithium Ion Batteries. *Angew. Chem., Int. Ed.* **2005**, *44*, 7085–7089.
- (2) Dedryvère, R.; Laruelle, S.; Gruegeon, S.; Poizot, P.; Gonbeau, D.; Tarascon, J.-M. Contribution of X-ray Photoelectron Spectroscopy to the Study of the Electrochemical Reactivity of CoO toward Lithium. *Chem. Mater.* **2004**, *16*, 1056–1061.
- (3) Liu, J.; Xia, H.; Lu, L.; Xue, D. Anisotropic Co₃O₄ Porous Nanocapsules toward High-Capacity Li-Ion Batteries. *J. Mater. Chem.* **2010**, *20*, 1506–1510.
- (4) Chen, Y. M.; Yu, L.; Lou, X. W. D. Hierarchical Tubular Structures Composed of Co₃O₄ Hollow Nanoparticles and Carbon Nanotubes for Lithium Storage. *Angew. Chem., Int. Ed.* **2016**, *55*, 5990–5993.
- (5) Dunn, B.; Kamath, H.; Tarascon, J.-M. Electrical Energy Storage for the Grid: a Battery of Choices. *Science* **2011**, *334*, 928–935.
- (6) Wang, H.-g.; Zhang, X.-b. Designing Multi-Shelled Metal Oxides: towards High Energy-Density Lithium-Ion Batteries. *Sci. China Mater.* **2016**, *59*, 521–522.
- (7) Li, W.; Zeng, L.; Wu, Y.; Yu, Y. Nanostructured Electrode Materials for Lithium-Ion and Sodium-Ion Batteries via Electrospinning. *Sci. China Mater.* **2016**, *59*, 287–321.
- (8) Wu, Z.-S.; Ren, W.; Wen, L.; Gao, L.; Zhao, J.; Chen, Z.; Zhou, G.; Li, F.; Cheng, H.-M. Graphene Anchored with Co₃O₄ Nano-particles as Anode of Lithium Ion Batteries with Enhanced Reversible Capacity and Cyclic Performance. *ACS Nano* **2010**, *4*, 3187–3194.
- (9) Pei, L.; Jin, Q.; Zhu, Z.; Zhao, Q.; Liang, J.; Chen, J. Ice-Templated Preparation and Sodium Storage of Ultrasmall SnO₂ Nanoparticles Embedded in Three-Dimensional Graphene. *Nano Res.* **2015**, *8*, 184–192.
- (10) Miao, C.; Liu, M.; He, Y.-B.; Qin, X.; Tang, L.; Huang, B.; Li, R.; Li, B.; Kang, F. Monodispersed SnO₂ Nanospheres Embedded in Framework of Graphene and Porous Carbon as Anode for Lithium Ion Batteries. *Energy Storage Mater.* **2016**, *3*, 98–105.
- (11) Su, D.; Dou, S.; Wang, G. Mesocrystal Co₃O₄ Nanoplatelets as High Capacity Anode Materials for Li-Ion Batteries. *Nano Res.* **2014**, *7*, 794–803.
- (12) Lai, H.; Li, J.; Chen, Z.; Huang, Z. Carbon Nanohorns as a High-Performance Carrier for MnO₂ Anode in Lithium-Ion Batteries. *ACS Appl. Mater. Interfaces* **2012**, *4*, 2325–2328.
- (13) Kim, J. M.; Huh, Y. S.; Han, Y.-K.; Cho, M. S.; Kim, H. J. Facile Synthesis Route to Highly Crystalline Mesoporous γ-MnO₂ Nanospheres. *Electrochem. Commun.* **2012**, *14*, 32–35.
- (14) Li, L.; Nan, C.; Lu, J.; Peng, Q.; Li, Y. α-MnO₂ Nanotubes: High Surface Area and Enhanced Lithium Battery Properties. *Chem. Commun.* **2012**, *48*, 6945–6947.
- (15) Li, Z.; Kong, D.; Zhou, G.; Wu, S.; Lv, W.; Luo, C.; Shao, J.-J.; Li, B.; Kang, F.; Yang, Q.-H. Twin-Functional Graphene Oxide: Compacting with Fe₂O₃ into a High Volumetric Capacity Anode for Lithium Ion Battery. *Energy Storage Mater.* **2017**, *6*, 98–103.
- (16) Bai, J.; Li, X.; Liu, G.; Xiong, S. Unusual Formation of ZnCo₂O₄ 3D Hierarchical Twin Microspheres as a High-Rate and Ultralong-Life Lithium-Ion Battery Anode Material. *Adv. Funct. Mater.* **2014**, *24*, 3012–3020.
- (17) Wang, T.; Zhu, J.; Chen, Y.; Yang, H.; Qin, Y.; Li, F.; Cheng, Q.; Yu, X.; Xu, Z.; Lu, B. Large-scale production of silicon nanoparticles@graphene embedded in nanotubes as ultra-robust battery anodes. *J. Mater. Chem. A* **2017**, *5*, 4809–4817.
- (18) He, C.; Wu, S.; Zhao, N.; Shi, C.; Liu, E.; Li, J. Carbon-Encapsulated Fe₃O₄ Nanoparticles as a High-Rate Lithium Ion Battery Anode Material. *ACS Nano* **2013**, *7*, 4459–4469.
- (19) Zhu, J.; Wang, T.; Fan, F.; Mei, L.; Lu, B. Atomic-Scale Control of Silicon Expansion Space as Ultrastable Battery Anodes. *ACS Nano* **2016**, *10*, 8243–8251.
- (20) Guo, J.; Chen, L.; Wang, G.; Zhang, X.; Li, F. In situ synthesis of SnO₂–Fe₂O₃@polyaniline and their conversion to SnO₂–Fe₂O₃@C composite as fully reversible anode material for lithium-ion batteries. *J. Power Sources* **2014**, *246*, 862–867.
- (21) Zhang, X.; Chen, H.; Xie, Y.; Guo, J. Ultralong life lithium-ion battery anode with superior high-rate capability and excellent cyclic stability from mesoporous Fe₂O₃@TiO₂ core–shell nanorods. *J. Mater. Chem. A* **2014**, *2*, 3912–3918.
- (22) Wang, J.; Zhang, Q.; Li, X.; Xu, D.; Wang, Z.; Guo, H.; Zhang, K. Three-Dimensional Hierarchical Co₃O₄/CuO Nanowire Heterostructure Arrays on Nickel Foam for High-Performance Lithium Ion Batteries. *Nano Energy* **2014**, *6*, 19–26.
- (23) Bai, Y.; Liu, W.; Yu, C.; Wang, T.; Feng, J.; Xiong, S. One-Pot Solvothermal Synthesis of ZnO@α-Co(OH)₂ Core–Shell Hierarchical Microspheres with Superior Lithium Storage Properties. *J. Phys. Chem. C* **2016**, *120*, 2984–2992.
- (24) Zhou, W.; Cheng, C.; Liu, J.; Tay, Y. Y.; Jiang, J.; Jia, X.; Zhang, J.; Gong, H.; Hng, H. H.; Yu, T.; Fan, H. J. Epitaxial Growth of Branched α-Fe₂O₃/SnO₂ Nano-Heterostructures with Improved Lithium-Ion Battery Performance. *Adv. Funct. Mater.* **2011**, *21*, 2439–2445.
- (25) Wang, Y.; Xu, J.; Wu, H.; Xu, M.; Peng, Z.; Zheng, G. Hierarchical SnO₂–Fe₂O₃ Heterostructures as Lithium-Ion Battery Anodes. *J. Mater. Chem.* **2012**, *22*, 21923–21927.
- (26) Hou, L.; Lian, L.; Zhang, L.; Yuan, C.; Zhang, X. Self-Sacrifice Template Fabrication of Hierarchical Mesoporous Bi-Component-Active ZnO/ZnFe₂O₄ Sub-Microcubes as Superior Anode towards High-Performance Lithium-Ion Battery. *Adv. Funct. Mater.* **2015**, *25*, 238–246.

- (27) Li, M.; Yin, Y.-X.; Li, C.; Zhang, F.; Wan, L.-J.; Xu, S.; Evans, D. G. Well-Dispersed Bi-Component-Active CoO/CoFe₂O₄ Nanocomposites with Tunable Performances as Anode Materials for Lithium-Ion Batteries. *Chem. Commun.* **2012**, *48*, 410–412.
- (28) Rai, A. K.; Gim, J.; Thi, T. V.; Ahn, D.; Cho, S. J.; Kim, J. High Rate Capability and Long Cycle Stability of Co₃O₄/CoFe₂O₄ Nanocomposite as an Anode Material for High-Performance Secondary Lithium Ion Batteries. *J. Phys. Chem. C* **2014**, *118*, 11234–11243.
- (29) Hu, L.; Zhong, H.; Zheng, X.; Huang, Y.; Zhang, P.; Chen, Q. CoMn₂O₄ Spinel Hierarchical Microspheres Assembled with Porous Nanosheets as Stable Anodes for Lithium-ion Batteries. *Sci. Rep.* **2012**, *2*, 986.
- (30) Zhang, W.; Li, Z.; Gu, H.; Li, Y.; Zhang, G.; Zhang, F.; Fan, X. L-Proline Covalently Anchored on Graphene Oxide as an Effective Bifunctional Catalyst for Ketene Forming Reaction. *Chem. Eng. Sci.* **2015**, *135*, 187–192.
- (31) Safaei-Ghommi, J.; Masoomi, R.; Hamadanian, M.; Naseh, S. Magnetic Nanoscale Core–Shell Structured Fe₃O₄@l-Proline: an Efficient, Reusable and Eco-friendly Nanocatalyst for Diastereoselective Synthesis of Fulleropyrrolidines. *New J. Chem.* **2016**, *40*, 3289–3299.
- (32) Safaei-Ghommi, J.; Zahedi, S. l-Proline-Functionalized Fe₃O₄ Nanoparticles as a Novel Magnetic Chiral Catalyst for the Direct Asymmetric Mannich Reaction. *Appl. Organomet. Chem.* **2015**, *29*, 566–571.
- (33) Zhang, L.; He, R.; Gu, H.-C. Oleic Acid Coating on the Monodisperse Magnetite Nanoparticles. *Appl. Surf. Sci.* **2006**, *253*, 2611–2617.
- (34) Ren, Y.; Iimura, K.-i.; Kato, T. Structure of Barium Stearate Films at the Air/Water Interface Investigated by Polarization Modulation Infrared Spectroscopy and π -A Isotherms. *Langmuir* **2001**, *17*, 2688–2693.
- (35) Lin, H. B.; Rong, H. B.; Huang, W. Z.; Liao, Y. H.; Xing, L. D.; Xu, M. Q.; Li, X. P.; Li, W. S. Triple-Shelled Mn₂O₃ Hollow Nanocubes: Force-Induced Synthesis and Excellent Performance as the Anode in Lithium-Ion Batteries. *J. Mater. Chem. A* **2014**, *2*, 14189–14194.
- (36) Zhang, X.; Qian, Y.; Zhu, Y.; Tang, K. Synthesis of Mn₂O₃ Nanomaterials with Controllable Porosity and Thickness for Enhanced Lithium-Ion Batteries Performance. *Nanoscale* **2014**, *6*, 1725–1731.
- (37) Cong, H.-P.; Xin, S.; Yu, S. H. Flexible Nitrogen-Doped Graphene/SnO₂ Foams Promise Kinetically Stable Lithium Storage. *Nano Energy* **2015**, *13*, 482–490.
- (38) Du, N.; Chen, Y.; Zhai, C.; Zhang, H.; Yang, D. Layer-by-Layer Synthesis of γ -Fe₂O₃@SnO₂@C Porous Core–Shell Nanorods with High Reversible Capacity in Lithium-Ion Batteries. *Nanoscale* **2013**, *5*, 4744–4750.
- (39) Liu, S.; Wang, R.; Liu, M.; Luo, J.; Jin, X.; Sun, J.; Gao, L. Fe₂O₃@SnO₂ Nanoparticle Decorated Graphene Flexible Films as High-Performance Anode Materials for Lithium-Ion Batteries. *J. Mater. Chem. A* **2014**, *2*, 4598–4604.
- (40) Pan, L.; Wang, K.-X.; Zhu, X.-D.; Xie, X.-M.; Liu, Y.-T. Hierarchical Assembly of SnO₂ Nanowires on MnO₂ Nanosheets: a Novel 1/2D Hybrid Architecture for High-Capacity, Reversible Lithium Storage. *J. Mater. Chem. A* **2015**, *3*, 6477–6483.
- (41) Guo, J.; Zhu, H.; Sun, Y.; Tang, L.; Zhang, X. Flexible Foams of Graphene Entrapped SnO₂–Co₃O₄ Nanocubes with Remarkably Large and Fast Lithium Storage. *J. Mater. Chem. A* **2016**, *4*, 16101–16107.
- (42) Demir-Cakan, R.; Hu, Y.-S.; Antonietti, M.; Maier, J.; Titirici, M.-M. Facile One-Pot Synthesis of Mesoporous SnO₂ Microspheres via Nanoparticles Assembly and Lithium Storage Properties. *Chem. Mater.* **2008**, *20*, 1227–1229.
- (43) Wang, H.; Cui, L.-F.; Yang, Y.; Casalongue, H. S.; Robinson, J. T.; Liang, Y.; Cui, Y.; Dai, H. Mn₃O₄–Graphene Hybrid as a High-Capacity Anode Material for Lithium Ion Batteries. *J. Am. Chem. Soc.* **2010**, *132*, 13978–13980.
- (44) Jang, B. Z.; Liu, C.; Neff, D.; Yu, Z.; Wang, M. C.; Xiong, W.; Zhamu, A. Graphene Surface-Enabled Lithium Ion-Exchanging Cells: Next-Generation High-Power Energy Storage Devices. *Nano Lett.* **2011**, *11*, 3785–3791.
- (45) Laruelle, S.; Gruegeon, S.; Poizot, P.; Dollé, M.; Dupont, L.; Tarascon, J.-M. On the Origin of the Extra Electrochemical Capacity Displayed by MO/Li Cells at Low Potential. *J. Electrochem. Soc.* **2002**, *149*, A627–A634.
- (46) Yang, S.; Feng, X.; Ivanovici, S.; Müllen, K. Fabrication of Graphene-Encapsulated Oxide Nanoparticles: towards High-Performance Anode Materials for Lithium Storage. *Angew. Chem., Int. Ed.* **2010**, *49*, 8408–8411.
- (47) Lee, S. W.; Yabuuchi, N.; Gallant, B. M.; Chen, S.; Kim, B.-S.; Hammond, P. T.; Shao-Horn, Y. High-Power Lithium Batteries from Functionalized Carbon-Nanotube Electrodes. *Nat. Nanotechnol.* **2010**, *5*, 531–537.
- (48) Wu, Z.-S.; Sun, Y.; Tan, Y.-Z.; Yang, S.; Feng, X.; Müllen, K. Three-Dimensional Graphene-Based Macro- and Mesoporous Frameworks for High-Performance Electrochemical Capacitive Energy Storage. *J. Am. Chem. Soc.* **2012**, *134*, 19532–19535.
- (49) Wei, W.; Yang, S.; Zhou, H.; Lieberwirth, I.; Feng, X.; Müllen, K. 3D Graphene Foams Cross-Linked with Pre-Encapsulated Fe₃O₄ Nanospheres for Enhanced Lithium Storage. *Adv. Mater.* **2013**, *25*, 2909–2914.
- (50) Lai, C.; Wu, Z.; Gu, X.; Wang, C.; Xi, K.; Kumar, R. V.; Zhang, S. Reinforced Conductive Confinement of Sulfur for Robust and High-Performance Lithium–Sulfur Batteries. *ACS Appl. Mater. Interfaces* **2015**, *7*, 23885–23892.
- (51) Wang, D.; Yang, J.; Li, X.; Geng, D.; Li, R.; Cai, M.; Sham, T.-K.; Sun, X. Layer by Layer Assembly of Sandwiched Graphene/SnO₂ Nanorod/Carbon Nanostructures with Ultrahigh Lithium Ion Storage Properties. *Energy Environ. Sci.* **2013**, *6*, 2900–2906.
- (52) Xu, X.; Tan, H.; Xi, K.; Ding, S.; Yu, D.; Cheng, S.; Yang, G.; Peng, X.; Fakeeh, A.; Kumar, R. V. Bamboo-Like Amorphous Carbon Nanotubes Clad in Ultrathin Nickel Oxide Nanosheets for Lithium-Ion Battery Electrodes with Long Cycle Life. *Carbon* **2015**, *84*, 491–499.
- (53) Zhang, G.; Yu, L.; Wu, H. B.; Hoster, H. E.; Lou, X. W. D. Formation of ZnMn₂O₄ Ball-In-Ball Hollow Microspheres as a High-Performance Anode for Lithium-Ion Batteries. *Adv. Mater.* **2012**, *24*, 4609–4613.
- (54) Jiang, J.; Li, Y.; Liu, J.; Huang, X.; Yuan, C.; Lou, X. W. D. Recent Advances in Metal Oxide-based Electrode Architecture Design for Electrochemical Energy Storage. *Adv. Mater.* **2012**, *24*, 5166–5180.